Carbon 161 (2020) 758–771

Contents lists available at ScienceDirect

Carbon

journal homepage: www.elsevier.com/locate/carbon

Strategic design of magnetic carbonaceous nanocomposites and its application as multifunctional adsorbent

Laís Helena Sousa Vieira [a, b], Carla Manuela Sganzerla Sabino [a], Francisco Holanda Soares Júnior [a, c], Janaina Sobreira Rocha [a, b], Manuela Oliveira Castro [d], Rafael Silva Alencar [e], Luelc Souza da Costa [f], Bartolomeu Cruz Viana [g], Amauri Jardim de Paula [h], João Maria Soares [d], Antônio Gomes Souza Filho [a, i], Larissa Otubo [j], Pierre Basílio Almeida Fechine [b], Anupama Ghosh [a, i, **], Odair Pastor Ferreira [a, *]

[a] Laboratório de Materiais Funcionais Avançados (LaMFA), Departamento de Física, Universidade Federal do Ceará, Campus do Pici, Fortaleza, Ceará, Brazil
[b] Grupo de Química de Materiais Avançados (GQMat), Departamento de Química Analítica e Físico-Química, Universidade Federal do Ceará, Fortaleza, Ceará, Brazil
[c] Departamento de Ensino, Instituto Federal do Ceará, Limoeiro do Norte, Ceará, Brazil
[d] Centro de Síntese e Análise de Materiais Avançados (CSAMA), Departamento de Física, Universidade do Estado do Rio Grande do Norte, Mossoró, Rio Grande do Norte, Brazil
[e] Grupo de Espectroscopia Eletrônica e Vibracional, Faculdade de Física, Universidade Federal do Pará, Belém, Pará, Brazil
[f] Instituto de Química, Universidade Estadual de Campinas, Campinas, São Paulo, Brazil
[g] Laboratório de Física dos Materiais (FisMat), Departamento de Física & Pós-Graduação em Ciência e Engenharia dos Materiais, Universidade Federal do Piauí, Teresina, Piauí, Brazil
[h] Solid-Biological Interface Group (SolBIN), Departamento de Física, Universidade Federal do Ceará, Campus do Pici, Fortaleza, Ceará, Brazil
[i] Central Analítica, Universidade Federal do Ceará, Campus do Pici, Fortaleza, Ceará, Brazil
[j] Centro de Ciências e Tecnologia de Materiais (CCTM), Instituto de Pesquisas Energéticas e Nucleares, São Paulo, São Paulo, Brazil

ARTICLE INFO

Article history:
Received 24 November 2019
Received in revised form
23 January 2020
Accepted 23 January 2020
Available online 26 January 2020

Keywords:
Biomass
Hydrothermal carbonization
Magnetic nanoparticles
Iron oxides
Activated carbon and Dye removal

ABSTRACT

Magnetic carbonaceous nanocomposites (MCN) were prepared by hydrothermal carbonization (HTC) of a carbohydrate in the presence of Fe^{3+}, followed by thermal treatment with KOH for simultaneous activation and magnetization. The precursor formed (IOCN) in the HTC process contained iron oxide nanoparticles encapsulated in the hydrochar matrix. The thermochemical parameters of the activation (temperature and IOCN/KOH mass-ratio) were varied to achieve an increase of the specific surface area along with formation of magnetic phases in MCN compared to IOCN. Activation temperature was found to be responsible for the structural and morphological properties of the MCNs whereas the IOCN/KOH mass-ratio controlled the porosity. The magnetic properties of the MCNs originated from the formation of Fe_3O_4 and Fe^0 phases, which are encapsulated in the carbonaceous material. The MCNs were tested for adsorption of methylene blue (MB) dye, followed by magnetic separation. The MCN, produced in the optimized conditions, showed a specific surface area of 766 $m^2\ g^{-1}$, magnetization of 8 emu g^{-1} and a MB adsorption capacity of 570 mg g^{-1}. Detailed kinetic and isotherm studies of MB adsorption were also performed. The methodology of simultaneous activation and magnetization to generate MCNs, presented here, could be extended to obtain new multifunctional carbon-based nanocomposite adsorbent starting from different biomasses.

© 2020 Elsevier Ltd. All rights reserved.

1. Introduction

As the humankind is facing the challenges to rethink their actions and options in order to revert back the environmental damage caused by ever-growing civilization, the synthesis and utilization of

* Corresponding author.
** Corresponding author. Laboratório de Materiais Funcionais Avançados (LaMFA), Departamento de Física, Universidade Federal do Ceará, Campus do Pici, Fortaleza, Ceará, Brazil.
E-mail addresses: anupama@fisica.ufc.br (A. Ghosh), opferreira@fisica.ufc.br (O.P. Ferreira).

https://doi.org/10.1016/j.carbon.2020.01.089
0008-6223/© 2020 Elsevier Ltd. All rights reserved.

new, advanced, functional carbon materials has drawn enormous attention because of the following facts: rich chemistry leading to endless combinations for smart designing [1], use of renewable and sustainable sources for mass-production [2], light-weight and non-toxicity suitable for various energy and environment-related applications, such as fuel [3], supercapacitor [4], adsorption [5,6], sensing [7,8], catalysis [9] among others. Their surface properties, such as high specific surface area, elevated porosity, surface oxygen functionality etc., makes them susceptible towards further modification and functionalization [10], opening up the possibility of anchoring other functional systems, thus leading to a multifunctional hybrid system targeted to increase the efficiency as well as scope of the resulting material [11]. One such example is magnetic carbonaceous nanocomposite (MCN) [12], where inorganic magnetic nanoparticles such as magnetic ferrites (**M**Fe_2O_4, where **M** denotes a divalent metal such as Mn^{2+}, Fe^{2+}, Co^{2+}, Cu^{2+}, Zn^{2+}etc) [13–17] decoration is achieved by *in-situ* growth [14] or *ex-situ* mixing [18] of these magnetic nanoparticles on to the intrinsically functionalized carbonaceous surface [19] or surface-functionalization mediated anchoring [20]. These MCNs show synergistic effect in their respective properties, which amplifies their potential in the fields of application such as environment remediation [21] electrochemical sensing [22], catalysis [23], biomolecule separation [24], drug delivery [25] etc. Amongst the newest water purification treatments [26], adsorption of pollutants such as various dyes and harmful metal ions by MCN, followed by magnetic separation using an external magnetic field [27] has been achieved even at an industrial-scale bio-reactor set-up [28]. The carbon coating over magnetic core in MCN protects it from physical contact with the oxidative environment without affecting the magnetic properties, which makes it useable (for many cycles) for acidic or basic effluent systems [29] or other reactive medium.

Activated carbon, a porous and high-surface area carbonaceous material, often used for adsorption [30] can be easily decorated with magnetic nanoparticles, with marginal reduction in the surface area and porosity, as the magnetic nanoparticles gets into fewer pores [31], turning it susceptible to easy, fast and efficient magnetic separation after successfully removing harmful metal ions [32], dyes [33] or other organic molecules [34]. A large variety of dye is disposed in ground water every year, mainly by innumerous textile industries [35] which has a lot of harmful effect on the aquatic life [36]. Methylene blue (MB) is a cationic, water soluble, planer dye, used in dying paper, nylon, polyester etc., which, congested in smaller scale, can cause severe abdominal pain, diarrhea nausea etc. Its prolonged exposure may create lungs infection and cancer [37]. Along with the facility of easy separation under external magnetic field, MCN shows better adsorption with MB compared to the non-magnetic activated carbon because of the presence of −OH bonds on the surface of these magnetic oxide nanoparticles, which create a coulombic interaction with the cationic dyes combined with the usual π-π interaction with the otherwise neutral carbon phase [38]. After the dye adsorption and magnetic separation, MCN could be regenerated in a Fenton-like oxidation process, where the dye can be degraded in smaller harmless organic compounds on simple addition of H_2O_2 [39].

Large-scale, cost-effective synthesis of MCN can be achieved by greener routes such as hydrothermal [40] and microwave [41] treatment of simple carbon-rich molecules such as glucose [40] or sugar [18] or even abundant biomasses such as sugarcane bagasse [41], acorn shell [42], corncob [43] etc. in presence of iron salts, followed by thermal treatment, where impregnated iron compounds acts as an activation agent as well as the seeding element for the growth of magnetic nanocrystals [44]. Addition of mild chemical oxidants, such as K_2CO_3 [45] or $ZnCl_2$ [42], or even CO_2 activation [46] can improve the surface area a great deal with retention of magnetic property. The reaction parameters such as temperature, time of the thermal treatment, magnetic precursor to carbon precursor ratio as well as the amount of activation agent can be optimized to obtain the best result in terms of dye removal from wastewater [47].

Although the MCN prepared by *in-situ* co-precipitation of magnetic oxide nanoparticles onto the AC surface by stoichiometric reaction have elevated surface area, the inorganic magnetic phase remains exposed, leading to the loss of the magnetic property by areal oxidation [14]. The alternate strategy of covering magnetic cores with thin carbon layer by hydrothermal carbonization (HTC) in presence of glucose avoid this kind of oxidation, but remains low in surface area and porosity, thereby having low adsorption capacity [18,40]. To overcome this barrier, in this study, an eco- and environment-friendly design strategy of multifunctional MCN materials has been proposed starting from glucose as a model carbon precursor and $Fe(NO_3)_3$ as the magnetic precursor. An iron oxide nanocomposite precursor (IOCN) was prepared by hydrothermal carbonization, followed by low-temperature thermal treatment, aided by KOH, for simultaneous activation and magnetization. The advantage of the proposed methodology was to pre-encapsulate the iron oxide phase in the precursor nanocomposite (hydrochar). The best reaction condition in the terms of specific surface area, magnetization and MB removal capacity was investigated varying the temperature of thermal treatment and IOCN/KOH mass ratio. All the MCN samples produced were thoroughly characterized: CHN elemental analysis and thermogravimetric analysis (TGA) gave the compositional details; Fourier-transform infrared spectroscopy (FTIR) and Raman spectroscopy as well as the X-ray diffraction (XRD) depicted the crystal and molecular structure; electron microscopy (SEM and TEM) and N_2 adsorption-desorption study provided the morphological and textural details, respectively, and sample vibrating magnetometer (VSM) along with the electron paramagnetic resonance spectroscopy (EPR) measurements established the magnetic characterization. MB was chosen as a model dye for elucidating the adsorption behaviors of the MCNs. Detailed adsorption study was performed with the MCN with best MB uptake capacity found. After the adsorption, the adsorbent-adsorbate (MCN-MB) composite was successfully separated from the solution using a simple bar-magnet. The MCNs showed excellent efficiency as multifunctional adsorbent material with a high MB uptake, which is very promising in further possibilities, such as adsorption of the harmful metal ions and/or complex pharmaceutical products and immobilization enzymes for catalysis.

2. Experimental section

2.1. Materials

All chemical were used as received: anhydrous glucose ($C_6H_{12}O_6$, 99.98 %), iron (III) nitrate nonahydrate ($[Fe(NO_3)_3]\cdot 9H_2O$, 98.0 %) and potassium hydroxide (KOH, 85.0 %) were purchased from Vetec; hydrochloric acid (HCl, 37.0 %) and methylene blue ($C_{16}H_{18}ClN_3S$) were purchased from Alphatec and Sigma-Aldrich, respectively. All experiments were carried out using ultrapure mili-Q® water.

2.2. Preparation of magnetic carbonaceous nanocomposites

The magnetic nanocomposites were prepared using hydrothermal carbonization, followed by thermochemical activation. In the first step, iron oxide containing carbonaceous nanocomposite precursor was synthesized by the HTC of glucose (1.00 g), $[Fe(NO_3)_3]\cdot 9H_2O$ (0.30 g) and 40 mL ultrapure water. The ratio of iron (III) nitrate and glucose used was established thinking of a

nominal Fe/C molar ratio in the nanocomposite of 0.1 (i.e. 10 %). After the complete solubilization of the raw materials, the pH was measured to be 2.0. The solution was transferred to a Teflon-lined stainless steel autoclave (50 mL capacity), heated up to 190 ± 10 °C in muffle furnace for 9 h. After that, the autoclave was cooled to room temperature and the pH of the suspension was measured to be 3.5. The solid-liquid separation was carried out by vacuum filtration using PVDF membrane of pore size 0.45 μm. The resulting black solid was washed with ultrapure water until the filtrate became colorless with measured pH to be between 5 and 6. The residue was oven dried at 70 ± 10 °C. The sample was identified as iron oxide carbonaceous nanocomposite (IOCN). A reference sample, named as hydrochar, was prepared in the same conditions but, without iron (III) nitrate for comparison purpose.

In order to produce the MCNs the precursor IOCN was thermochemically activated using KOH. In this process, 2.0 and 4.0 g of KOH were dissolved in 10 mL ultrapure water under ice bath and added 1.00 g of IOCN (to maintain the IOCN/KOH mass ratio of 1:2 and 1:4). The suspension was magnetically stirred for 0.5 h and afterwards the mixture was dried at 105 °C for 12 h. The resulting material was carefully ground and transferred to an alumina combustion boat. The thermal treatment was carried out in a tubular furnace (EDG, model FTHI/20) under moderate nitrogen flow at 500 and 700 °C for 1 h with a heating rate of 10 °C min^{-1}. After cooling under nitrogen environment, the sample was first washed using 0.5 mol L^{-1} HCl, followed by ultrapure water until the pH was close to 7. The resulting solid was dried at 70 °C for 24 h. The final products were identified as MCN-*xy*, (magnetic carbonaceous nanocomposites) where $x = 5$ and 7, representing the temperatures, 500 and 700 °C, respectively and $y = 2$ and 4, representing the IOCN/KOH mass ratio, 1:2 and 1:4.

2.3. Characterization

Carbon, nitrogen and hydrogen contents of the samples were determined using an elemental analyzer, PerkinElmer, 2400 Series II CHNS/O. To determine the percentage of iron phases in nanocomposites, the thermogravimetric analysis were carried out using an Netzsch STA 449 F3 equipment from 30 to 800 °C under an air flow of 50 mL min^{-1} and heating rate of 10 °C min^{-1}. The mass of the sample used was around 10 mg. Raman spectra were recorded in the range of 100–2000 cm^{-1} using the LabRam HR equipment from Horiba, with an excitation laser source of 633 nm. The laser was focused with a 50 × magnification objective lens and the signal was dispersed by a grating of 1800 grooves mm^{-1}. ATR-FTIR spectra were recorded on a Vertex 70v spectrometer equipped with a Platinum ATR accessory, diamond ATR module. The spectra were obtained under vacuum, in the mid-infrared region (400–4000 cm^{-1}) with 2 cm^{-1} resolution and 128 scans. Powder X-ray diffraction (XRD) patterns were obtained with a X'Pert PRO MPD diffractometer from PANalytical, using Co-K_α radiation ($\lambda = 1.789$ Å) generated at 40 mA and 40 kV. The equipment was calibrated with LaB_6 standard sample and the diffractograms were carried out using steps of 0.013° in the range of 10–85° (2θ). Rietveld refinement was carried out on this XRD data using MAUD (Material Analysis Using Diffraction), an open-source software. SEM images were obtained using a Quanta 450 FEG microscope manufactured by FEI. For SEM analysis the crushed and sieved samples were pulverized on carbon tape attached to aluminum sample holders and coated with gold by sputtering using an ES Quorum QT150. For elemental mapping, energy dispersive X-ray spectroscopy (EDS) was recorded using X-ray detector model 150 from Oxford coupled to Quanta 450 FEG microscope. Transmission electron microscopy (TEM) images were obtained with a MSC JEOL TEM-2100 200 kV microscope, equipped with a CCD (TVip–16 MP) and TV (GatanES500W). In order to do TEM, the samples were dispersed in isopropyl alcohol and drop-casted onto carbon-coated or collodion-coated 400 mesh copper grids and allowed to dry overnight before analysis. Textural properties were analyzed from nitrogen adsorption-desorption isotherms at −196 °C using a Belsorp mini II surface area analyzer from BEL JAPAN, INC. Prior to measurements, the samples were outgassed at 105 °C for 14 h under N_2 flow. Specific surface area (S_{BET}) was calculated using Brunauer-Emmette-Teller (BET) method; micropores specific surface area (S_{mic}) was calculated by the t-plot method; pore size distribution curve was obtained by Barrett-Joyner-Halenda (BJH) method and micropores volume calculated by MP analysis. Magnetic measurements of the samples were performed with a Perron MT 4070 Vibrating Sample Magnetometer (VSM) at room temperature and 9 K. Adjustments were made for room temperature magnetization curves using Equation (1) (the Langevin function):

$$M = M_S\ [\coth\ (\mu H / K_B T) - \ (K_B T / \mu H)] \quad (1)$$

where M is magnetization, M_s is the saturation magnetization, μ is the magnetic moment, H is the applied magnetic field, k_B is the Boltzmann constant and T is the absolute temperature.

The electron paramagnetic resonance spectrum (EPR) was measured at room temperature using a Bruker instrument, model EMXmicro. The instrument was operated under the following conditions: microwave frequency: 9.695 and 9.715 GHz; power: 152.7 and 187.2 mW; phase modulation: 0 and 210°; conversion time: 61 and 119 ms; number of scans: 1 and 2.

2.4. Adsorption experiments with MB

The preliminary adsorption test was carried out to evaluate the adsorption capacity for the as-prepared samples: hydrochar, IOCN, MCN-52, MCN-54, MCN-72 and MCN-74. In order to do so, batch adsorption experiments were performed by adding 20 mg of each material to 20 mL of the 100 mg L^{-1}MB solution (dosage 1 g L^{-1}) in a 50 mL Erlenmeyer flask and constantly shaken (orbital shaker) at 200 rpm for 4 h. As the samples MCN-72 and MCN-74 removed all the dye from the solution, a more concentrated MB solution (500 mg L^{-1}) were used for these samples. After the adsorption, the solid adsorbate-absorbent mass was magnetically separated using a magnet with nominal intensity of 0.28 T. The apparent clear solution was then centrifuged at 12 000 rcf for 15 min (Eppendorf, model 5418 R), in order to get rid of any remanent solid for no interference in UV–Visible absorption analysis. The supernatant solutions were analyzed in a UV–visible spectrophotometer (Specord 250, from Analytik Jena). MB concentrations were determined from Lambert-Beer's law using a calibration curve considering the MB-λ_{max} at 665 nm. The absorbed amounts of MB, q_e (mg per gram of the adsorbent) were calculated using Equation (2):

$$q_e = \frac{V\ (C_o - \ C_e)}{W} \quad (2)$$

where V (L) is the volume of the MB solution; C_o and C_e (mg L^{-1}) are the initial and equilibrium concentration of MB, respectively; W (g) is the mass of the samples.

The effect of time on the adsorption was studied (kinetic study) using only the MCN-74 sample because it showed the best result for MB adsorption at room temperature. In a typical batch experiment, 20 mL of the 500 mg L^{-1} MB solution was mixed with 20 mg of MCN-74 (dosage of 1 g L^{-1}) in 50 mL flasks and the contact time was varied between 1 and 300 min. The same experimental procedures mentioned before were used for solid-liquid separation

and determination of MB concentration. The amount of MB adsorbed on the MCN-74 at time t (min) was calculated from Equation (3):

$$q_t = \frac{V\ (C_o - C_t)}{W} \quad (3)$$

where C_o (mg L^{-1}) is the initial concentration of MB; C_t is the liquid phase concentration of MB at predefined time.

The effect of initial concentration of the dye on the adsorption (equilibrium studies) was studied as 20 mg of MCN-74 was added to 20 mL (dosage 1 g L^{-1}) of MB solutions with different concentrations (50–1300 mg L^{-1}). The flasks were constantly shaken at 200 rpm for 120 min. After the solid-liquid separation by the aforementioned process, the final MB concentrations were measured using UV–visible spectroscopy, as stated above. All these experiments were conducted in triplicate at room temperature. In order to dig deeper, the nonlinear kinetic models: pseudo-first-order (PFO), pseudo-second-order (PSO), Elovich and particle diffusion were fitted to the kinetic data whereas the nonlinear models of Langmuir, Freundlich, and Temkin were tested as adsorption isotherm. All the non-linear equations are shown in supplementary information.

3. Results and discussion

3.1. Compositional and structural analysis of the MCNs

The carbon precursor glucose, in the presence of the ferric salt during HTC process, transforms into carbonaceous material (hydrochar) containing encapsulated iron oxide/hydroxide nanoparticles (Fe_2O_3/FeOOH) forming iron oxide carbonaceous nanocomposite (as seen in the TEM images presented as Figs. S1e and f) [48,49]. The mechanism of hydrochar formation from carbohydrates is already well-established in the literature [48,50–52]. However, the *in-situ* formation mechanism of the nanocomposite involving both inorganic and hydrochar phases is not yet fully established. Based on the fact that the pH of the reaction mixture increases during the hydrothermal process (initial pH = 2.0 and final pH = 3.5), we propose the formation mechanism as follows: the nucleation of iron oxide/hydroxide nanoparticles starts following the reactions 4 and 5 which starts interacting with the first nuclei of the carbonaceous material (about 5 nm) formed from glucose decomposition [51]. Then, particle growth from a few nanometers to microns occurs via coalescence of nanometric nuclei followed by agglomeration. These iron oxide carbonaceous nanocomposite (IOCN) were used as the precursor for simultaneous activation/magnetization.

$$Fe^{3+}_{(aq)} + 3H_2O_{(l)} \rightarrow Fe(OH)_{3(aq)} + 3H^{+}_{(aq)} \quad (4)$$

$$Fe(OH)_{3(aq)} \rightarrow FeO(OH)_{(s)} + H_2O_{(l)} \rightarrow Fe_2O_{3(s)} + H_2O_{(l)} \quad (5)$$

Hydrothermal carbonization of glucose (or other carbohydrates) leads to the formation of a carbon-rich material (50–70 % by mass) and the elemental composition depends on the reaction conditions such as temperature, initial pH of the medium and reaction time [53–55]. In order to compare the properties of the precursor nanocomposite, a HTC was also performed under the same conditions, but without the addition of ferric nitrate. The elemental composition (CHN analysis) and the mass of the inorganic residue obtained from TGA analysis are presented in Table 1. The hydrochar produced by hydrothermal carbonization of glucose in absence of ferric nitrate has 62.2 % of carbon (C) and 4.2 % of hydrogen (H). This result indicates that the precursor dehydration was not complete and the carbonaceous matrix also contains O, along with C and H, as observed by other authors [50,52,53,56].

Table 1
Chemical properties of the nanocomposites: carbon (C), hydrogen (H), nitrogen (N) content from CHN elemental analysis and iron (Fe) content, calculated from the TGA residue of the samples.

Samples	Elemental composition			TGA residue[a]	
	C (%)	H (%)	N (%)	Fe_2O_3 (%)	Fe (%)[b]
Hydrochar	62.2	4.2	0.0	–	0.0
IOCN	55.6	4.1	1.4	17.1	12.0
MCN-52	45.0	2.8	1.3	16.8	11.8
MCN-54	47.7	2.3	1.3	30.3	21.2
MCN-72	50.0	2.1	1.9	21.4	15.0
MCN-74	47.0	3.3	0.6	16.7	11.7

[a]Quantified as Fe_2O_3.
[b] Calculated from TGA residue.

Iron oxide carbonaceous nanocomposite (IOCN) has lower C concentration (55.6 %) than hydrochar (Table 1). The relative reduction of carbon content in nanocomposite is related to the presence of iron oxide. However, when the H/C molar ratios were analyzed for hydrochar (0.80) and IOCN (0.87), only a slight change in the values was observed, indicating a similar degree of carbonization for both the samples. Unlike hydrochar, the precursor nanocomposite has small amount nitrogen (1.4 %) in its composition. The presence of nitrogen can be due to the presence of nitrate ion in the reaction mixture as a counter ion of Fe^{3+} which gets incorporated in the carbonaceous network as nitrogenous organic compounds or nitrogen functional groups [53,54].

The starting condition of preparation of IOCN was chosen to have a nominal Fe/C concentration of 10 % (w:w), as stated in the experimental section. TGA curve was used to assess the actual Fe/C concentration in the final product. The iron content (12.0 %) was calculated from the residual mass (17.1 %) measured in the TGA curve, considering the composition of the inorganic residue as entirely Fe_2O_3 (Table 1). Such consideration is consistent with the red color observed for the residue which is very characteristic of Fe_2O_3. Also, it can be seen from phase diagram of iron, at higher concentration of oxygen (as the TGA was done under an air flow), at 800 °C (the temperature range, up to which the TGA was done) only hematite (Fe_2O_3) phase can be present [57]. Thus, it was verified that the actual iron content in IOCN was close to the nominal value predicted in the preparation scheme and thereby, can be used for subsequent thermochemical activation step. Additionally, the spatial distribution of carbon, oxygen and iron in the sample IOCN was verified by EDS-elemental mapping (as seen in the EDS-SEM image, Figs. S1a–d). The sample IOCN has spherical particles of the order of a few microns, rich in evenly distributed carbon and oxygen and lower proportion of iron, as well as nanoparticles containing iron, oxygen and carbon.

IOCN was submitted to thermochemical treatment with the activation agent KOH in order to prepare magnetic carbonaceous nanocomposite (MCN), containing magnetic iron phases. The objective was to simultaneously intensify the textural properties of the nanocomposite and promote the transformation of the non-magnetic iron oxide phase to magnetic iron phases. Regarding the elemental composition of the activated samples (MCN-*xy*), a reduction in carbon and hydrogen contents was observed when compared to the precursor nanocomposite and hydrochar (Table 1). Loss of hydrogen could be associated with the elimination of water and small organic molecules (e.g. methane) during thermal treatment. On the other hand, loss of carbon could be related to the high temperature reactions between carbon and iron oxide, as shown in reactions 6–11, where iron oxide acts as an oxidizing agent,

oxidizing structural carbon at high temperature to gaseous products as CO and CO_2 [58–62]. However, no clear correspondence could be made out with of the reaction parameters (temperature and mass ratio of the activating agent) to the final composition. After the reaction, the MCNs were washed with diluted HCl in order to get rid of the K_2CO_3 generated in the process (Reaction 10) as well as the unused KOH. In the presence of acid, effervescence was observed, suggesting the elimination of CO_2 (Reaction 11). A trace amount of nitrogen was observed in these MCN samples. This reinforces the possibility that, nitrogen being once incorporated in the carbonaceous matrix due to HTC in presence of nitrate ion, does not leave the carbon skeleton, even after the thermochemical treatment in different temperatures and remains in the final material.

$$6Fe_2O_{3(s)} + C_{(s)} \rightarrow 4Fe_3O_{4(s)} + O_{2(g)} \quad (6)$$

$$Fe_3O_{4(s)} + C_{(s)} \rightarrow 3FeO_{(s)} + CO_{(g)} \quad (7)$$

$$FeO_{(s)} + CO_{(g)} \rightarrow Fe_{(s)} + CO_{2(g)} \quad (8)$$

$$K^+_{(aq)} + OH^-_{(aq)} + C_{(s)} \rightarrow 2K_{(s)} + H_{2(g)} + K_2CO_{3(s)} \quad (9)$$

$$K_2CO_{3(s)} + 2\,C_{(s)} \rightarrow 2\,K_{(s)} + 3\,CO_{(g)} \quad (10)$$

$$K_2CO_{3(s)} + 2HCl_{(aq)} \rightarrow 2KCl_{(s)} + H_2O_{(l)} + CO_{2(g)} \quad (11)$$

The iron content in MCNs was calculated from TGA in a similar fashion and was found to be ranging from 11.7 to 21.2 % Activation of the precursor nanocomposite can generate a reducing environment during heat treatment, as described in Reactions 7 and 8, leading to reduced iron phases (e.g. Fe_3O_4 and Fe^0). In order to correctly identify the formed phases, X-ray powder diffraction (XRD) and electron paramagnetic resonance spectrum (EPR) were performed, as discussed further in this section and section 3.3. The spatial distribution of the elements: carbon, oxygen and iron in the microscopic range of the MCNs were investigated using EDS. A typical EDS mapping of a representative MCN sample, MCN-74, were illustrated in Fig. 1a–d, which shows a uniform distribution of carbon and oxygen throughout the matrix. However, the elemental map of iron (Fig. 1d) showed that, in addition to being homogeneously distributed throughout the matrix, there are regions with high intensity of Fe, that are not concurrent with the oxygen mapping (Fig. 1c), suggesting higher concentration of iron which can be due to the presence of elemental iron (Fe^o), formed in the reducing environment of the thermochemical process (Reaction 8).

Fig. S2 shows the X-ray diffractograms of hydrochar, IOCN and MCN-74 nanocomposites. The hydrochar presents a characteristic profile broad peak with low intensity in the region 15–35° (2θ), suggesting a low structural order carbonaceous matrix [63,64]. Similar profile was observed for the precursor nanocomposite IOCN, except for the presence of broad and low intensity peaks attributed to the hematite phase [(α-Fe_2O_3 with peaks centered at 39.0, 41.5, 47.2 and 74.6° (2θ), COD ID 9009782], a non-magnetic iron oxide. These peak profiles, corresponding to hematite phase, is characteristic of nanoparticles because their broad nature [64–66], which corroborates with the TEM images of this nanocomposite (Figs. S1e and f). The presence of hematite phase in the carbonaceous matrix was quantified to be 17.1 % by thermogravimetric analysis (Table 1). The X-ray diffractogram of the representative MCN sample (MCN-74), shows narrower and more intense peaks for inorganic phases, but still superimposed on to a low-

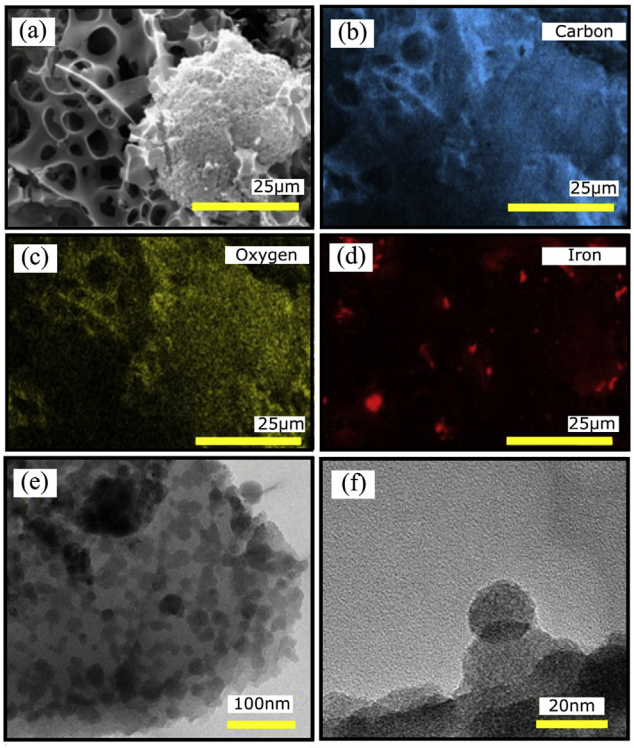

Fig. 1. (a) SEM image and EDS elemental mapping of MCN-74 sample showing the presence of (b) carbon, (c) oxygen and (d) iron; (e) TEM image of MCN-74 sample, showing uniform distribution of iron oxide nanoparticles throughout the carbonaceous matrix. (A colour version of this figure can be viewed online.)

crystalline material diffraction profile with a broad and large peak between 22 and 35° (2θ), attributing to the carbonaceous phase, which remains nanocrystalline with low graphitization, even after the thermal treatment at 700 °C. On the other hand, the narrower and more intense peaks of the inorganic phases suggest that the iron oxide and related phases becomes more crystalline in thermochemical treatment. The more intense and fine nature of some peaks also suggests the formation of more crystalline iron phases [66] which could be agglomerated in carbonaceous matrix as suggested by EDS Fe mapping (Fig. 1d) and backscattering electron (BSE)-SEM and TEM (Fig. S5). Due to the possibility of having multiple phases in the inorganic part, a structural refinement was performed using the Rietveld method to aid in the identification of these phases (Fig. S3 and Table S1). From this refinement, the following magnetic phases were identified: Fe_3O_4 (magnetite) with peaks centered at 35.1, 41.5, 50.6, 67.2 and 74.2° (2θ) (COD ID 9002318); metallic iron, Fe^o with peaks centered at 52.4 and 77.3° (2θ), (COD ID 9016518) and FeO (Wustite) with peaks centered at 41.9, 50.0 and 71.6° (2θ) (COD ID 9002670), with relative concentrations of 64.0, 29.1 and 6.9 %, respectively. Thus, KOH activation produced Fe_3O_4 and Fe^o magnetic phases from non-magnetic α-Fe_2O_3, possibly having FeO as the intermediate phase according to Reactions 6 to 8. The formation of metallic iron had also been suggested by regions with high signal for Fe without corresponding signal for O found in the EDS elemental mapping as stated earlier (Fig. 1d).

In order to achieve a better understanding of the short-range interaction, especially in the carbonaceous phase, measurements of the FTIR and Raman spectroscopy of nanocomposites were performed (Fig. 2). The Raman spectra of all the samples in the low wavenumber range (100-400 cm^{-1}) are shown in Fig. 2a. All of

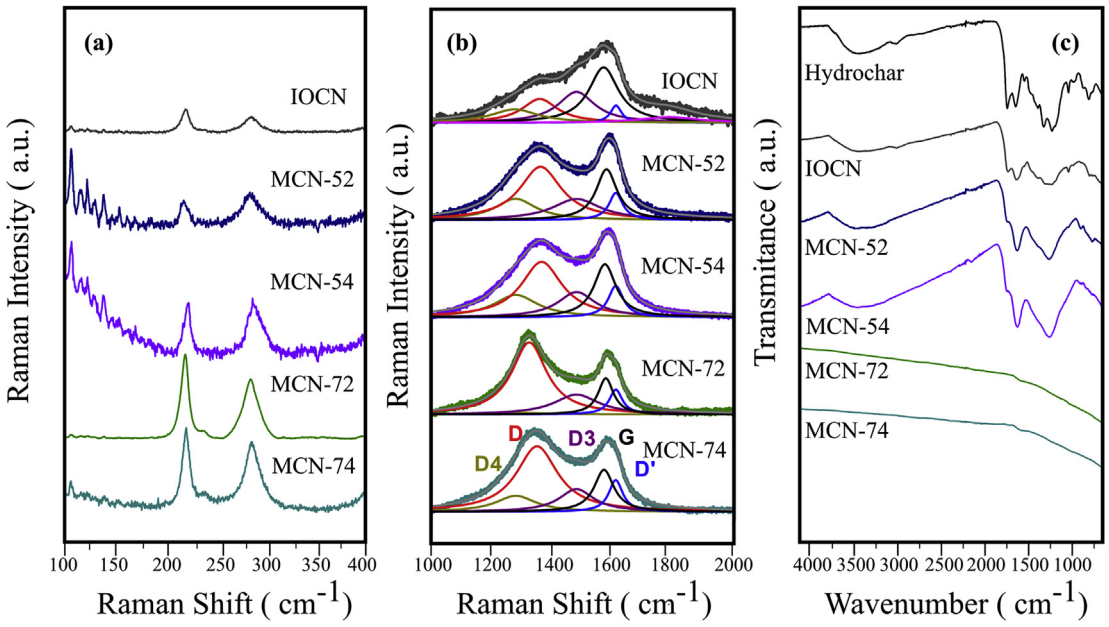

Fig. 2. Raman spectra of nanocomposites at (a) low wavenumber range (100-400 cm^{-1}) and at (b) high wavenumber range 1000–2000 cm^{-1}; (c) FTIR spectra for the nanocomposites in mid-IR region (650-4000 cm^{-1}). (A colour version of this figure can be viewed online.)

them showed spectral signature bands of iron oxide at 220 and 285 cm^{-1} [67], thus suggesting that the oxide nanoparticles are already present in the precursor nanocomposite, which is also evidenced by TEM images (Figs. S1e and f). But a careful observation reveals that with the increment of reaction temperature from 500 to 700 °C, the signal-noise ratio of these bands increases as well as the relative intensities (relative to the carbon G band). These facts suggest that with the increase of reaction temperature the formation of the iron oxide crystals in the carbon matrix is more pronounced. Fig. S4 presents the full range Raman spectra (100-2000 cm^{-1}) of the sample MCN-74, showing all the Raman bands corresponding to the iron oxide as well as the carbon-rich phase. The bands centered around 218, 282, 394, 489 and 600 cm^{-1} are spectral signature of the iron oxide phase [67,68]. The bands centered around 218 and 489 cm^{-1} can be assigned to the two A_{1g} modes whereas the bands centered around 282, 394 and 600 cm^{-1} can be assigned as the E_g modes of the hematite phase [67–69]. We did not see bands that could be attributed to iron phases identified in the XRD patterns (Fe_3O_4, FeO and Fe^o). However, all MCN samples are magnetic, as they get attracted by a magnet, as seen in the experiment as well as the magnetic data (see section 3.3). As the hematite phase is weak ferromagnetic, it must be accompanied with the magnetic phases [70,71]. Indeed, reduced iron phases are thermodynamically less stable and it is prone to *in-situ* degradation on heating promoted by laser irradiation. As the Raman spectra was collected with a substantial power laser beam, probably the magnetite phase (found in more percentage in the sample) is changing to hematite and we were unable to see the signature of this phase in Raman measurements. This phenomenon has been noted before [72].

The high frequency region (1000-2000 cm^{-1}) Raman Spectra provides information about the carbonaceous part of nanocomposites (Fig. 2b). All spectra exhibited bands centered at 1348 cm^{-1} (D band) and 1580 cm^{-1} (G band) suggesting the coexistence of more ordered (graphitized) and disordered (amorphous) domains. Specifically, the D band (1348 cm^{-1}) indicates the presence of structural defects, related to sp^3-type bonding, while the G band (1580 cm^{-1}) refers to sp^2-type bonding, characteristic of graphitic carbon [61,62]. The G band was already observed in the nanocomposite IOCN, but much broader and diffuse, suggesting heterogeneity in the carbonaceous domains formed during the HTC process. Also, the XRD pattern of IOCN showed high structural disorder (Fig. S2) which corroborates with the non-identification of the orderly domain through Raman spectroscopy. On the other hand, the D and G bands in the thermal treated samples become more evident (Fig. 2b). The relative degree of graphitization of nanocomposites can be estimated by the I_D/I_G ratio, as shown in Table S3. There is an increase of the graphitization degree in the carbonaceous matrix from activation at 500 and 700 °C. The G band correspond to the degenerate in-plane E_{2g} optical mode at the center of the Brillouin zone. The D band and D′ bands are Raman active in defective graphitic materials owing to defect-induced double resonance Raman scattering processes [73]. The D4 and D3 bands are present in highly defective carbons like carbon black (CB), and have been assigned to the presence of amorphous carbon (D3) and of hydrocarbon or aliphatic moieties connected on graphitic basic structural units (D4) [74,75]. From the analysis of the intensity ratio of the D, D′, D3 and D4 bands to the G band, it is observed that the increase in temperature promotes the increase of defects (higher I_D/I_G) in the carbonaceous structure. It is worth noting that increasing the IOCN to KOH ratio in the synthesis scheme initiates a downward trend in the I_D/I_G ratio. The amount of amorphous carbon (estimated by I_{D3}/I_G) does not appear to change significantly, which justifies the existence of amorphous phase even with increase of temperature. Thus, Raman spectroscopy indicates that the different activation parameters influence mainly the carbonaceous phase of nanocomposites.

The effect of activation temperature on nanocomposite structure can be further evidenced by the FTIR spectra (Fig. 2c). The spectral profiles of hydrochar and precursor nanocomposite (IOCN) are typical of carbonaceous material obtained by HTC process of carbohydrates. Both spectra have a broadband centered at 3300 cm^{-1}, assigned to O–H stretching vibration of hydroxyl groups. The aliphatic part of the carbonaceous chains is evidenced by the low and medium intensity bands in the regions centered at 2918, 1430 and 1350 cm^{-1}, which can be attributed to the C–H

stretching and deformation modes. The bands centered at 1700 cm^{-1} and 1606 cm^{-1} for the hydrochar (1691 and 1593 cm^{-1} for IOCN, respectively) can be assigned to the C═O stretching of carboxylic acid groups and the C═C stretching of aromatic domain, respectively. The relative shifts of these bands to lower wavelengths to IOCN spectrum compared to hydrochar indicates interactions between the carbonaceous and inorganic phase which is another indirect evidence of the fact that the iron oxide nanoparticles are encapsulated in the carbonaceous matrix, as seen in the TEM images (Figs. S1e and f). The bands at 850–750 cm^{-1}can be assigned to aromatic C–H out-of-plane bending vibrations, confirming the presence of aromatic domains. The remaining bands in the region of 1300–1000 cm^{-1} can be attributed to the C–O and C–O–C stretches of remaining glycosidic rings or hydrocarbon chains present in the hydrochar [66–69].

The spectra of activated samples at 500 °C (MCN-52 and MCN-54), regardless of the activation ratio used, show bands related to C–H and C–O vibrations with lower relative intensities compared to the precursor ones. This finding suggests the reduction of this type of chemical bonds in activated samples due to the elimination of small molecules such as H_2O, CO, CO_2 or low molecular weight hydrocarbons. In addition, a relative increase in the intensity of the C═C stretching (at 1585 cm^{-1}) is observed, indicating an increase in the aromatic domains in the carbonaceous matrix. These results are consistent with those observed for Raman spectroscopy. However, for samples activated at 700 °C (MCN-72 and MCN-74) there is a drastic reduction in the intensity of all the bands, suggesting the elimination of practically all chemical groups, thus indicating a high degree of aromatization of these samples.

3.2. Morphological and textural properties of the nanocomposites

Our objective with thermochemical activation was to simultaneously perform the phase transformation of the precursor iron oxide in enhancing the magnetic properties, as well as enhancing the textural properties of the nanocomposites. From the morphological point of view, drastic changes have been observed as a function of the activation parameters, which is illustrated in Fig. 3 as SEM images in various magnifications. In the SEM images of the IOCN, spherical particles of the order of a few microns (from 1 to 5 μm) along with nanoparticle clusters are shown. Micrometric spherical particles are typical of hydrochar obtained from HTC of carbohydrates [76]. On the other hand, the iron oxide nanoparticles (of the order of 10 nm) can be seen as encapsulated in the carbonaceous matrix (Figs. S1e and f). Elemental mapping of Fe (Fig. S1d) suggests that iron oxide nanoparticles are present in a lesser extent in carbonaceous microspheres.

When thermochemical activation was performed at 500 °C (samples MCN-52 and MCN-54), regardless IOCN/KOH mass ratio, the well-defined spherical morphology of the carbonaceous part as well as the nanoparticle agglomerates is maintained. However, some of those spheres showed coalescence in some regions and that the surface appeared rough (Fig. 3). These observations suggest the formation of the first cavities in the carbonaceous phase leading to a porous structure compared to the almost non-porous precursor, as corroborated by the N_2 adsorption-desorption results (see Fig. S6). Increasing the activation temperature to 700 °C (samples MCN-72 and MCN-74), independent of the IOCN/KOH mass ratio, it was possible to observe drastic modification of the morphology. In these conditions the spherical particles become almost rare to find out and the whole sample appears to be very porous. In the SEM images obtained by backscattering electrons (BSE), which emphasis on atomic number contrast, clusters with much brighter contrast can be identified everywhere in the representative sample (MCN-74) which are identified as the iron related phase (Figs. S5a–c). These micron sized inorganic agglomerates are distributed throughout the carbonaceous matrix. However, the TEM images (Fig. 1e and f) show nanoparticles of iron phases distributed for all carbonaceous phase. Furthermore, it is worth noting that both BSE and TEM images suggest that the iron phases are embedded/encapsulated in the carbonaceous matrix (also see Figs. S5d–f), and this fact is of great importance because that would prevent the rapid oxidation of the reduced iron ($Fe_3O_4$and Fe^0) phases that are responsible for nanocomposite magnetism leading to desirable applicability. This feature also enables the MCN to be more versatile in severe chemical conditions, like, acidic or basic conditions.

The effect of the thermochemical activation (temperature and IOCN/KOH mass ratio) on the textural properties of nanocomposites was investigated by N_2 adsorption-desorption at −196 °C. As can be seen in the adsorption-desorption isotherm

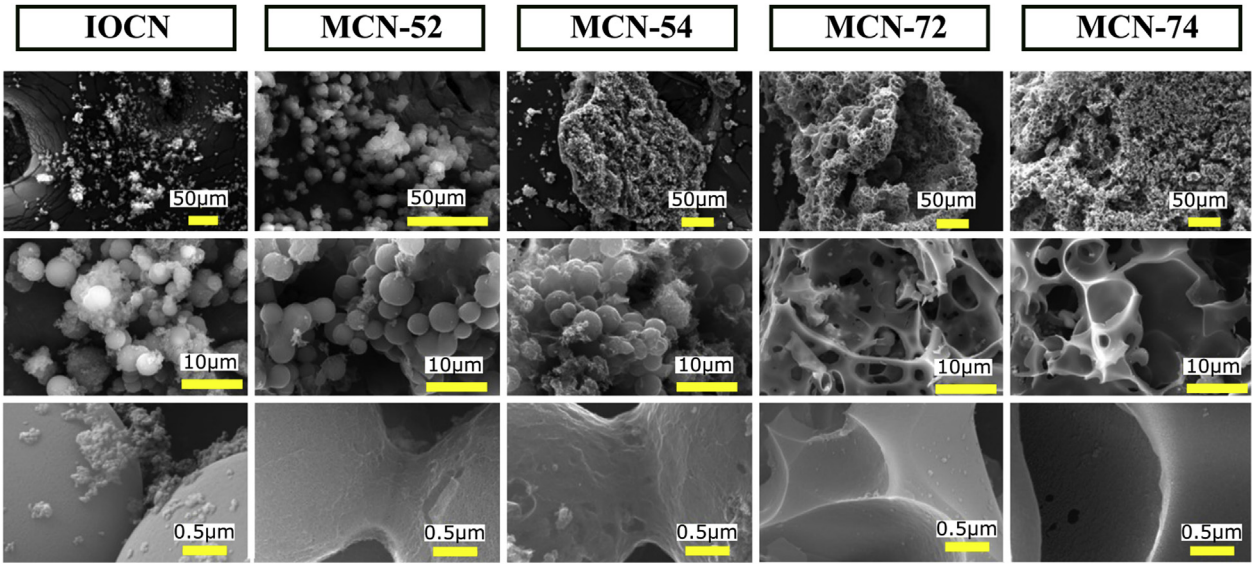

Fig. 3. SEM images of the nanocomposites showing gradual transformation from microsphere to open porous structure with temperature. (A colour version of this figure can be viewed online.)

curves (Fig. S6a), it was not observed a marked amount of adsorbed N_2 on hydrochar and IOCN samples and these samples present similar pore size distribution profiles (Fig. S6b). According to the IUPAC classification [77], hydrochar and IOCN present type III isotherm. These isotherms are typical to a non-porous solid. The adsorbed molecules are grouped in more favorable locations on the surface and does not diffuse in. This behavior is characteristic of hydrochars [63,78,79]. The very low surface area also justifies the fact that these samples are almost non-porous or macroporous. For the samples MCN-52 and MCN-72 type IV isotherms are observed [77], which indicates the presence of mesoporous, evidenced by the sudden fall in the desorption branch in the region of p/p_0 equal to 0.4. Isotherms for the samples MCN-54 and MCN-74 can be assigned to type I [77], typical of microporous solids (Fig. S6a). For MCN-54 and MCN-74 the presence of a hysteresis loop above $p/p_0 = 0.4$ suggest presence of substantial amount of mesoporous [80,81], as supported by ratio of mesoporous/microporous volume (V_{meso}/V_{micro}) calculated from BET and MP analysis (Table 2). On the other hand, the samples MCN-54 and MCN-74 do not show this type of large hysteresis loop, which is also reflected by the low V_{meso}/V_{micro} value, shown in Table 2. The pore size distribution of MCN-52 and MCN-72 are very similar, just as that of MCN-54 and MCN-74 (Fig. S6). So, it can be stated that the distribution of the pores and their overall nature is dependent of the precursor to activation agent mass ratio.

The textural properties of the samples obtained through adsorption-desorption isotherms are shown in Table 2. In general, hydrochar and IOCN are solids with a low specific surface area (S_{BET}) of 19.6 and 37.3 $m^2\ g^{-1}$, respectively, as predicted by their isothermal profile analysis. When thermochemical treatments were applied, we observed an expressive increase in the S_{BET} areas of the nanocomposites in the range from 320 to 760 $m^2\ g^{-1}$. Also, we determined the specific surface area of micropores (S_{micro}) using the t-plot method. The MCNs shows S_{micro} in the range from 434 to 1580 $m^2\ g^{-1}$, the largest S_{micro} being was observed for the sample MCM-74 (Table 2). The average pore diameter obtained by the BJH method (considering meso and micropore range) indicates that all of them (MCN) showed average pore diameter ranging from 3.1 to 4.9 nm. It is noteworthy that the average pore diameter for samples obtained with IOCN/KOH mass ratios 1:4 were smaller than those obtained with 1:2, suggesting once again the formation of higher number of micropores for samples with increment of IOCN/KOH ratio. Also, higher micropore volume was observed for these samples as observed from the micropore analysis (MP) method (Table 2). This is logical because with increment of amount of KOH in the reaction mixture, the extent of oxidation of the structural carbon increases, leading to generation of more gaseous elements like CO and CO_2, and they create more microporous structure while escaping the system. Thus, amongst the different conditions applied for formation of MCNs, the MCN formed at 700 °C and IOCN/KOH ratio 1:4 (MCN-74) showed highest specific surface area, highest micropore specific surface area, greater total pore volume and greater total micropore volume. Naturally, it showed a very good potential of being used as a multifunctional nanocomposite adsorbent.

3.3. Magnetic properties

The magnetic properties of nanocomposites were evaluated by vibrating sample magnetometer (VSM) measurents (Fig. 4a). A typical paramagnetic behavior was observed for the IOCN sample with the magnetization curve being a straight line, suggesting the formation of only hematite phase (Fe_2O_3). The room temperature magnetization curves for the activated nanocomposites (MCNs) showed hysteresis with good symmetry and moderate magnetization ranging from 2.6 to 8 emu g^{-1} (Fig. 4a). Such values are characteristic of ferrimagnetic materials. Although X-ray diffraction

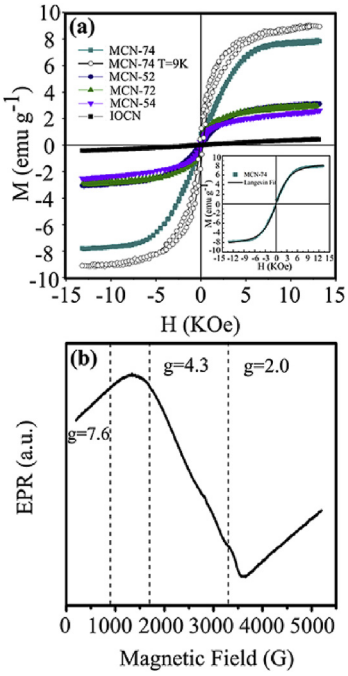

Fig. 4. (a) Magnetic hysteresis loops of the nanocomposites at room temperature and 9 K in zero-field-cooling mode. The inset of the figure shows magnetic hysteresis loop of the sample MCN-74 at room temperature adjusted to the Langevin function (b) EPR spectra of MCN-74 at room temperature. (A colour version of this figure can be viewed online.)

Table 2
Textural properties from N_2adsorption-desorption isotherms at −196 °C for all the nanocomposites.

Sample	S_{BET}[a] (m^2g^{-1})	S_{micro}[b] (m^2g^{-1})	Total pore volume (cm^3g^{-1})	Average pore diameter (nm)	Micropore volume[c] (cm^3g^{-1}) MP	Total mesopore volume [d](cm^3g^{-1})	$\frac{V_{meso}}{V_{micro}}$
Hydrochar	19.6	[e]	0.038	[e]	[e]	[e]	[e]
IOCN	37.3	[e]	0.094	[e]	[e]	[e]	[e]
MCN-52	319.5	434.2	0.391	4.9	0.144	0.247	1.7
MCN-54	298.0	534.5	0.255	3.4	0.197	0.103	0.5
MCN-72	489.3	894.7	0.542	4.4	0.260	0.282	1.1
MCN-74	766.0	1580.1	0.604	3.1	0.545	0.059	0.05

[a] Total specific surface is calculated by BET method ($p/p_0 = 0.99$).
[b] Micropore specific surface area calculated by t-plot method.
[c] Calculated by MP plot method.
[d] Calculated by BJH methods.
[e] Not applied.

(Fig. S3) indicates the presence of magnetite (Fe_3O_4) and metallic iron (Fe^0), which are ferrimagnetic and ferromagnetic materials, respectively, magnetization values were possibly reduced due to the presence of encapsulating carbon layers, a diamagnetic material over the magnetic phase attenuating saturation of magnetization [71–73] as indicated by the SEM and TEM images (Fig. S5). Magnetization hysteresis curve measured at 9 K for the MCN-74 sample in zero-field-cooling mode shows a 12 % increase in saturation magnetization compared to hysteresis curve measured at room temperature (Fig. 4a). The MCN-74 sample is composed of 64 % (Table S1) of Fe_3O_4 nanoparticles. Magnetite nanoparticles follow the Block law, which provides for an increase in M_s values at low temperatures [82].

The hysteresis of the MCN-52, MCN-54, MCN-72 and MCN-74 samples revealed small coercivities ranging from 0.05 to 0.19 kOe (Table S2). These values are may be characteristic of interacting superparamagnetic nanomaterials. To be classified as a non-interacting superparamagnetic, the nanomaterial must have practically zero coercivity (H_C~0) [83]. Thus, to verify if magnetic nanoparticles have superparamagnetic behavior, the Langevin function was used to adjust the magnetization curves [83]. The simulated data obtained by using the Langevin function in equation (1) are also given in inset in Fig. 4a. There is a near fit between experimental and theoretical values for MCN-74. For the other MCNs, an adjustment was not possible using the Langevin function. The behavior of MCN samples could be related to an inhomogeneous size distribution, where this magnetic property is compromised by the presence of particles having diameters above the superparamagnetic critical diameter. Moreover, the presence of other crystalline phases such as hematite, contributes to the deviation of superparamagnetic behavior. However, narrow hysteresis indicates that this material is easy to magnetize (soft material) and presents low coercivity. These magnetic properties make these MCNs suitable for using as a magnetic adsorbent material where these magnetic properties can be utilized to facilitate the solid-liquid separation step, as they can respond rapidly in the presence of the external magnetic field.

Electron paramagnetic resonance spectroscopy (EPR) was carried out aiming to complement the identification of the magnetic phases. The EPR spectrum of MCN-74 (Fig. 4b) obtained at room temperature revealed two broad gyroscopic resonance lines with gyroscopic factor g = 7.6 (898 G) and g = 2.0 (3400 G), respectively. Such resonances are characteristic of Fe^{3+} ions at tetrahedral and/or octahedral sites linked to oxygen atoms [74]. EPR spectra also suggest changes in the spectral line above 3300 G denoting factors g < 2, probably from Fe^{3+} compounds with spin moment S = 1/2, typical of the Fe_3O_4 phase [75]. The narrow resonance line, centered around 3440 G (g ~ 2.0), is related to Fe^{3+} ion exchange interaction, attributed to the Fe_3O_4 phase [83].Additionally, a second, much wider line between 2850 and 3600 G, centered around 3230 G, can be assigned to the metallic iron (Fe^0) nanoparticles [76]. Also, the line at 1700 G (g = 4.3) is related to wustite (FeO) phase containing Fe^{2+} [76]. Thus, the EPR results corroborate with the findings of XRD (Fig. S3 and Table S1) results.

3.4. Adsorption properties

The adsorption characteristics of the IOCN and MCN-52, MCN-54, MCN-72 and MCN-74 nanocomposites were initially evaluated. For comparisons, the hydrochar (sample without iron) was also tested. The concentration of MB solution was chosen to be 100 mg L^{-1} for preliminary tests with an equilibrium time of 4 h. The MCN-72 and MCN-74 samples showed complete discoloration of MB to this concentration and equilibrium time, suggesting that they have excellent adsorption capacity for MB (Figs. S7a and b). For them, a new test was performed under the same conditions using a concentration of 500 mg L^{-1}. They showed an adsorption capacity of 240.10 and 457.00 mg g^{-1}, respectively, which corresponds to 48 and 91 % removal of the dye (Figs. S7a and c). As the sample MCN-74 showed highest adsorption capacity amongst all the samples, corroborating with the excellent textural and porosity properties, further experiments were carried out with it to investigate the effect of reaction time and initial concentration of the dye on the adsorption phenomena at a constant temperature.

The adsorption profile of MB with increasing interaction time is given in Fig. 5a, which showed a rapid initial uptake owing to a concentration gradient of MB in the solution and the solid surface, followed by gradual rise leading to a site-saturation-induced quasi-equilibrium. The adsorption kinetic was investigated in order to understand the mechanism of attaining equilibrium through mass transfer and the experimentally obtained adsorption kinetics curve was fitted to the non-linear pseudo-first-order (PFO), pseudo-second-order (PSO) and Elovich kinetic models (equations are shown in Table S4) and the obtained kinetic parameters shown in Table 3 [14,41]. It was found out that the kinetic data best fits to the Elovich model (correlation coefficient, R^2 value = 0.9788) compared to PSO model (R^2 = 0.9066). The PFO model, which suggests diffusion through a boundary, does not show a good match with a very low R^2 value (0.7731). Also the experimental value of q_e (455.88 mg g^{-1}) matches much better with the calculated value

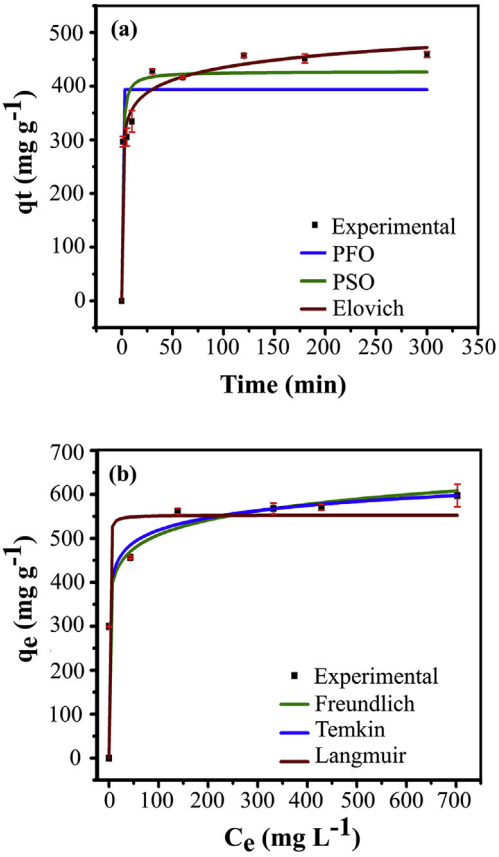

Fig. 5. (a) Kinetic study for MCN-74 with the initial concentration of MB being 500 mg L^{-1}, fitted in different non-linear kinetic models, such as, pseudo-first-order (PFO) (blue), pseudo-second-order (PSO) (green) and Elovich (wine); (b) Adsorption isotherm of MB onto MCN-74 at equilibrium time of 2 h (The initial concentrations of MB is varied from 50 to 1300 mg L^{-1}, fitted in different non-linear isotherm models, such as Langmuir (red), Freundlich (green) and Temkin (blue). Both the experiments (Kinetic and Isotherm) were carried out using a dosage of 1 g L^{-1} and conducted in triplicate at room temperature. (A colour version of this figure can be viewed online.)

Table 3
Kinetic parameters of MB adsorption on MCN-74 using the PFO, PSO, Elovich and particle diffusion models.

Models	Kinetic Parameters			
PFO	**k_1 (min^{-1})**		**q_e (mg g^{-1})**	**R^2**
	80.98		393.51	0.7731
PSO	**k_2 (g mg^{-1} min^{-1})**		**q_e (mg g^{-1})**	**R^2**
	0.003		427.18	0.9066
Elovich	**α (gm g^{-1} min^{-2})**		**β (gm g^{-1} min^{-1})**	**R^2**
	125720.16		0.0290	0.9788
Particle diffusion		**k_F(mg g^{-1} $min)^{1/2}$**	**C (mg g^{-1})**	**R^2**
	First step	296.61	~0	0.9948
	Second step	38.24	217.04	
	Third step	3.87	398.35	

when calculated using the PSO model (427.18 mg g^{-1}) compared to that with the PFO model (393.51 mg g^{-1}). The R^2 value for Elovich model as well as PSO model suggests non-uniformity of the adsorption process. MB being a cationic dye and MCN-74, having negative surface oxygen functional groups on carbonaceous phase, there is a high possibility of columbic type of interaction. But the MB being a planer aromatic molecule and MCN-74 having graphitic domains, as described in the Raman spectroscopy, also π-π interaction takes place between them, suggesting simultaneous presence of two types of interactions [14]. The PFO model describes the adsorption behavior of the system in terms of the adsorption capacity of the adsorbent. It can be noted that (Fig. 5a) the PFO curve accompany well the experimental data in the beginning, falling apart after some time. On the other hand, the PSO model takes into account on the adsorption behavior over the entire time range. These observations endorse the fact that the adsorption capacity of solid does not stay same throughout the time, in other words, there is a preference of filling the sites by MB molecules. The Elovich model is a rate equation based on adsorption capacity with parameters, which depends on the surface coverage and adsorption activation energy, gives the best fit, anyway.

Aiming to dig further into the adsorption mechanism as well as the identification of the rate controlling step, particle diffusion model was applied to the equilibrium data (equation are shown in Table S4) [41]. q_t is plotted against $t^{1/2}$ in the whole time range and shown in Fig. S8. A linear graphical q_t vs $t^{1/2}$ plot with zero intercept indicates intraparticle diffusion as the sole rate controlling step [84]. But in this case three straight lines can be fitted with different slopes and intercept with a very good fitting parameter ($R^2 = 0.9948$) which indicates three distinct step of the adsorption process with increasing boundary thickness (~0,217.04 and 398.35 mg g^{-1} for first, second and third step, respectively) and decreasing diffusion rate (296.61, 38.24 and 3.86 mg g^{-1} $min^{1/2}$ for first, second and third step, respectively). Looking at the microstructure and texture of MCN-74 found in the material characterization, these three steps can be assigned as (1) The first step, almost instantaneous external diffusion, caused the adsorbate gradient difference of MB in solution and solid, accompanied by the coulombic attraction between positively charged adsorbate and negatively charged adsorbent as well as the π-π interaction; (2) the second step as less fast, intraparticle diffusion into mesopores, owing to the fact that the sample MCN-74 contains a few mesopores and diffusion into mesopores are easy because of the larger size (3) the third and final step of slowest intraparticle diffusion into the micropores which is clearly the rate-limiting step in the sorption process [14]. Table S5 illustrates the kinetic parameters of the particle diffusion model.

From the kinetics data it had been seen that the adsorption reaches equilibrium at 120 min. MCN-74 was added with MB solutions of different concentrations (50–1300 mg L^{-1}) and stirred for 120 min to reach the equilibrium. Fig. 5b illustrates the MB uptake of MCN-74 as a function of equilibrium MB concentration (C_e). A steep rise of MB uptake can be observed with increase of C_o, owing to the greater mass transfer driving force at higher C_o, reaching a plateau at around 570 mg g^{-1}. However, with increasing initial concentration, the percent removal of MB decreases due to the higher number of competing MB molecules in the solution but lesser available active sites on the solid. At equilibrium state, the distribution of the adsorbates (MB) in the aqueous phase and solid phase was analyzed by fitting with different isotherm models: Langmuir, Freundlich and Temkin, to identify the most suitable one for the adsorption process [14]. The non-linear forms of these models are expressed in Table S5. The parameters by fitting the experimental data in these three non-linear isotherm equations are expressed in Table 4, which also provided information about adsorption mechanism, surface adherence and surface features. All of them show a fair match with the experimental data, especially both the Freundlich and Temkin models shows very high R^2 value (0.9922 and 0.9929 respectively) compared to Langmuir model ($R^2 = 0.9536$). That suggests, the adsorption process does not take place as uniform monolayer adsorption involving identical and energetically equivalent adsorption sites, rather a heterogeneous type of interaction with a non-uniform distribution of adsorption energy of different active sites, as depicted by Freundlich and Temkin model which assumes that the adsorption sites are distributed exponentially (Freundlich) or linearly (Temkin) with respect to the energy of adsorption. This is logical, assuming that, the nanocomposite has graphitic domains, capable of π-π interaction with the planer MB molecule involving lower adsorption energy as well as its negative surface charge is capable of columbic interaction with positively charged MB molecule, which has a higher energy of interaction. That can also depict the deviation of the experimental isotherm curve from the Langmuir depicted sharp "L" shaped curve. However, the feasibility of the adsorption can be expressed with a separation factor (R_L), obtained from the Langmuir isotherm (Table S5). For all the C_0 used in the experiments, the R_L values lie within 0 and 1, proving the adsorption of MB onto MCN-74 is a favorable process. The Freundlich isotherm also suggests the same as the value of $1/n_F$ is 0.092, which is less than 1, rendering it a favorable process. Also, the step-wise adsorption

Table 4
The fitting parameters for MB on MCN-74 using the Langmuir, Freundlich and Temkin adsorption models (the equilibrium time is 2 h).

Adsorption models	Parameters		
Langmuir	**K_L (L g^{-1})**	**q_m (mg g^{-1})**	**R^2**
	2.91	552.89	0.9536
Freundlich	**K_F (L mg^{-1})**	**n_F**	**R^2**
	332.16	10.83	0.9922
Temkin	**K_T (L mg^{-1})**	**B (J mol^{-1})**	**R^2**
	3710.90	0.612	0.9929

mechanism suggests intricate non-uniform nature of the interaction, involving the coulombic interaction as well as the π-π interaction between the adsorbate and absorbent, followed by diffusion into the pores hierarchically. Although, as the models were originally assumed for gas-phase reaction, there are a number of deciding factors, such as hydration forces, mass transport effects etc. are present in solid-liquid heterogeneous system which can affect those assumptions. The enhanced adsorption of MCN-74 can be attributed to the high surface area, enhanced porosity and presence of active adsorption sites. A brief comparison is presented in Table 5 between specific surface area values and MB dye adsorption capacity relative to values obtained in recent research on the development of magnetic activated carbon in different carbon sources. In the context of the multifunctional composite adsorbent, we can remove the MCN-74 sample from the solid-liquid mixtures by employing a magnet, as shown in Fig. S7b.

4. Conclusion

A rational two-step strategy involving hydrothermal carbonization, followed by thermochemical activation process, leading to simultaneous activation and magnetization, was employed to prepare multifunctional magnetic carbonaceous nanocomposites (MCN). The MCNs prepared are basically carbonaceous nanocomposites containing encapsulated magnetic nanoparticles. Such feature is extremely important for the application as multifunctional composite adsorbents (for adsorption and magnetic separation) avoiding premature oxidation of iron phases as well as the viability of the use in acidic/basic conditions. The iron oxide phase was encapsulated in the carbonaceous nanocomposite precursor in the first step by hydrothermal carbonization, with subsequent chemical activation with KOH as the second step, leading to textural properties intensification as well as generation of magnetic phases through iron oxide reduction. The temperature of the thermochemical activation process was varied (500 and 700 °C) as well as the precursor to activation agent mass ratio (1:2 and 1:4). The MCNs contained iron ranging from 11 to 21 %, quantified indirectly by TGA analysis with the phases recognized as Fe_3O_4, FeO and Fe°, indicated by XRD and EPR, encapsulated and distributed as nanoparticles in the carbonaceous matrix, indicated by the elemental mapping and TEM. Raman and IR spectroscopy showed the structural evolution, whereas SEM and N_2 adsorption-desorption showed the drastic influence of the reaction temperature on the morphology and textural properties of the carbonaceous phase. Also, N_2 adsorption-desorption indicated that precursor to activation agent mass ratio influence mainly in porosity of carbonaceous phase. All the MCNs were tested as multifunctional composite adsorbent against MB adsorption. With the best results (MB adsorption capacity of ~570 mg g^{-1}) obtained with MCN-72, detailed adsorption study was carried out. Presence of non-uniform adsorption sites was predicted by the isotherm modeling which surmises both coulombic and π-π type interaction between MCN-74 and MB molecules. Kinetic studies predict a multi-step adsorption mechanism involving fast charge-transfer, followed by slow pore-diffusion, with diffusion into micropores being the rate limiting step. After adsorption, the adsorbent phase was easily removed from the medium using a magnet rendering these MCNs as multifunctional composite adsorbents performing both the functions of efficient adsorbent and magnetic separation. The work presented here has great potential as it can be used as a model to obtain new multifunctional composite adsorbents starting from different biomasses, in extension.

Table 5
Comparison between the specific surface area (S_{BET}) and maximum equilibrium adsorption capacity (q_e) of various magnetic carbon nanocomposites (MCNs) found in recent literature.

Carbon source/Samples	S_{BET}(m^2 g^{-1})	q_e(mg g^{-1})	Refs.
Glucose/MCN-74	766.0	570.00	This work
Eucalyptus sawdust/MAC	645.23	228.22	[85]
Sugarcane bagasse/MSBAC	109.07	36.14	[41]
Sargassumoligocystum/ACSO/Fe_3O_4	126.77	60.60	[84]
Glucose/MPCM	480.32	56.44	[64]
Fruit residue/Fe_2O_3/C	764.11	>352.96	[39]
Disaccharide ($C_{12}H_{22}O_{11}$)/Fe_3O_4@C	27.65	52.6	[18]
Charcoal (commercial)/Fe_3O_4- charcoal	387.30	97.49	[14]
Corncob/MCA	153.89	163.93	[43]
Activated carbon (commercial)/M3	543.74	6.32	[86]

Declaration of competing interest

The authors declare that they have no known competing financial interests or personal relationships that could have appeared to influence the work reported in this paper.

CRediT authorship contribution statement

Laís Helena Sousa Vieira: Conceptualization, Data curation, Formal analysis, Investigation, Methodology, Software, Validation, Visualization, Writing - original draft, Writing - review & editing. **Carla Manuela Sganzerla Sabino:** Conceptualization, Data curation, Formal analysis, Investigation, Methodology, Software, Validation, Visualization, Writing - review & editing. **Francisco Holanda Soares Júnior:** Conceptualization, Data curation, Formal analysis, Investigation, Methodology, Resources, Software, Validation, Visualization, Writing - original draft, Writing - review & editing. **Janaina Sobreira Rocha:** Conceptualization, Data curation, Formal analysis, Investigation, Methodology, Software, Validation, Visualization, Writing - original draft, Writing - review & editing. **Manuela Oliveira Castro:** Conceptualization, Data curation, Formal analysis, Investigation, Methodology, Resources, Software, Validation, Visualization, Writing - original draft, Writing - review & editing. **Rafael Silva Alencar:** Conceptualization, Data curation, Formal analysis, Investigation, Methodology, Resources, Software, Validation, Visualization, Writing - original draft, Writing - review & editing. **Luelc Souza da Costa:** Conceptualization, Data curation, Formal analysis, Investigation, Methodology, Software, Validation, Visualization, Writing - review & editing. **Bartolomeu Cruz Viana:** Conceptualization, Formal analysis, Investigation, Methodology, Software, Validation, Visualization, Writing - review & editing. **Amauri Jardim de Paula:** Conceptualization, Formal analysis, Funding acquisition, Methodology, Resources, Software, Validation, Visualization, Writing - review & editing. **João Maria Soares:** Conceptualization, Data curation, Formal analysis, Investigation, Methodology, Resources, Software, Supervision, Validation, Visualization, Writing - original draft, Writing - review & editing. **Antônio Gomes Souza Filho:** Conceptualization, Data curation, Formal analysis, Funding acquisition, Investigation, Methodology, Resources, Software, Supervision, Validation, Visualization, Writing - original draft, Writing - review & editing. **Larissa Otubo:** Conceptualization, Data curation, Formal analysis, Investigation, Methodology, Software, Validation, Visualization, Writing - review & editing. **Pierre Basílio Almeida Fechine:** Conceptualization, Formal analysis, Funding acquisition, Investigation, Methodology, Project administration, Resources, Software, Supervision, Validation, Visualization, Writing - review & editing. **Anupama Ghosh:** Conceptualization, Data curation, Formal analysis, Investigation, Methodology, Resources, Software, Supervision, Validation, Visualization, Writing - original draft, Writing - review & editing. **Odair Pastor Ferreira:** Conceptualization, Data curation, Formal analysis,

Funding acquisition, Investigation, Methodology, Project administration, Resources, Software, Supervision, Validation, Visualization, Writing - original draft, Writing - review & editing.

Acknowledgement

LHSV thanks Coordination of Higher Education Personnel Improvement (Coordenação de Aperfeiçoamento de Pessoal de Nível Superior) – Finance Code 001. PBAF thanks National Council for Scientific and Technological Development (Conselho Nacional de Desenvolvimento Científico e Tecnológico) for financial support through Grant 408790/2016-4. OPF, AJP, and PBAF thank the Cearense Foundation for Scientific and Technological Development Support (Fundação Cearense de Apoio ao Desenvolvimento Científico e Tecnológico) for financial support through Grants PRONEX PR2-0101-00006.01.00/15 and PNE-0112-00048.01.00/16. OPF, AJP and AGSF also acknowledge funding from Cearense Foundation for Scientific and Technological Development (Programa Cientista Chefe). The authors acknowledge the Brazilian Nanotechnology National Laboratory (Proposal number TEM-24726) and Nuclear and Energy Research Institute (Instituto de Pesquisas Energéticas e Nucleares - IPEN) for the use of transmission electron microscopy facilities. Also, the authors are grateful to Analytical Center (Central Analítica -UFC/CTINFRA/MCTI-SISNANO/Pró-Equipamentos CAPES) for providing the electron scanning microscopes and X-ray laboratory at the Federal University of Ceará (Laboratório de raios-X da Universidade Federal do Ceará) for XRD facilities (CNPq Grant number 402561/2007-4).

Appendix A. Supplementary data

Supplementary data to this article can be found online at https://doi.org/10.1016/j.carbon.2020.01.089.

References

[1] S. Ravi, S. Vadukumpully, Sustainable carbon nanomaterials: recent advances and its applications in energy and environmental remediation, J. Environ. Chem. Eng. 4 (2016) 835–856, https://doi.org/10.1016/j.jece.2015.11.026.
[2] R. Mohammadinejad, S. Karimi, S. Iravani, R.S. Varma, Plant-derived nanostructures: types and applications, Green Chem. 18 (2016) 20–52, https://doi.org/10.1039/C5GC01403D.
[3] R.S. Costa, L.H.S. Vieira, A. Ghosh, A.M.S. Santos, O.P. Ferreira, B.C. Viana, Hydrothermal carbonization of waste babassu coconut biomass for solid fuel production, Rev. Virt. Quím. 11 (2019) 626–641, https://doi.org/10.21577/1984-6835.20190048.
[4] A. Ghosh, C. do Amaral Razzino, A. Dasgupta, K. Fujisawa, L.H.S. Vieira, S. Subramanian, R.S. Costa, A.O. Lobo, O.P. Ferreira, J. Robinson, M. Terrones, H. Terrones, B.C. Viana, Structural and electrochemical properties of babassu coconut mesocarp-generated activated carbon and few-layer graphene, Carbon N. Y. 145 (2019) 175–186, https://doi.org/10.1016/j.carbon.2018.12.114.
[5] A. Dasgupta, J. Matos, H. Muramatsu, Y. Ono, V. Gonzalez, H. Liu, C. Rotella, K. Fujisawa, R. Cruz-Silva, Y. Hashimoto, M. Endo, K. Kaneko, L.R. Radovic, M. Terrones, Nanostructured carbon materials for enhanced nitrobenzene adsorption: physical vs. chemical surface properties, Carbon N. Y. 139 (2018) 833–844, https://doi.org/10.1016/j.carbon.2018.07.045.
[6] A. Ghosh, K.S. Subrahmanyam, K.S. Krishna, S. Datta, A. Govindaraj, S.K. Pati, C.N.R. Rao, Uptake of H2 and CO2 by graphene, J. Phys. Chem. C 112 (2008) 15704–15707, https://doi.org/10.1021/jp805802w.
[7] A. Ghosh, D.J. Late, L.S. Panchakarla, A. Govindaraj, C.N.R. Rao, NO2 and humidity sensing characteristics of few-layer graphenes, J. Exp. Nanosci. 4 (2009) 313–322, https://doi.org/10.1080/17458080903115379.
[8] A. Ghosh, A.M. da Silva Santos, J.R. Cunha, A. Dasgupta, K. Fujisawa, O.P. Ferreira, A.O. Lobo, M. Terrones, H. Terrones, B.C. Viana, CO2 Sensing by in-situ Raman spectroscopy using activated carbon generated from mesocarp of babassu coconut, Vib. Spectrosc. 98 (2018) 111–118, https://doi.org/10.1016/j.vibspec.2018.07.014.
[9] Y. Zhai, Z. Zhu, S. Dong, Carbon-based nanostructures for advanced catalysis, ChemCatChem 7 (2015) 2806–2815, https://doi.org/10.1002/cctc.201500323.
[10] A. Gomathi, S.J. Hoseini, C.N.R. Rao, Functionalization and solubilization of inorganic nanostructures and carbon nanotubes by employing organosilicon and organotin reagents, J. Mater. Chem. 19 (2009) 988–995, https://doi.org/10.1039/B813570C.
[11] S. Mitra, S. Banerjee, A. Datta, D. Chakravorty, A brief review on graphene/inorganic nanostructure composites: materials for the future, Indian J. Phys. 90 (2016) 1019–1032, https://doi.org/10.1007/s12648-016-0841-x.
[12] M. Zhu, G. Diao, Review on the progress in synthesis and application of magnetic carbon nanocomposites, Nanoscale 3 (2011) 2748–2767, https://doi.org/10.1039/c1nr10165j.
[13] G. Akkaya Sayğılı, Synthesis, characterization and adsorption properties of a novel biomagnetic composite for the removal of Congo red from aqueous medium, J. Mol. Liq. 211 (2015) 515–526, https://doi.org/10.1016/j.molliq.2015.07.048.
[14] M.J.K. Ahmed, M. Ahmaruzzaman, A facile synthesis of Fe3O4–charcoal composite for the sorption of a hazardous dye from aquatic environment, J. Environ. Manag. 163 (2015) 163–173, https://doi.org/10.1016/j.jenvman.2015.08.011.
[15] J.C. Xu, P.H. Xin, Y.B. Han, P.F. Wang, H.X. Jin, D.F. Jin, X.L. Peng, B. Hong, J. Li, H.L. Ge, Z.W. Zhu, X.Q. Wang, Magnetic response and adsorptive properties for methylene blue of CoFe2O4/CoxFey/activated carbon magnetic composites, J. Alloys Compd. 617 (2014) 622–626, https://doi.org/10.1016/j.jallcom.2014.08.059.
[16] G. Zhang, J. Qu, H. Liu, A.T. Cooper, R. Wu, CuFe2O4/activated carbon composite: a novel magnetic adsorbent for the removal of acid orange II and catalytic regeneration, Chemosphere 68 (2007) 1058–1066, https://doi.org/10.1016/j.chemosphere.2007.01.081.
[17] B.B. Zhang, J.C. Xu, P.H. Xin, Y.B. Han, B. Hong, H.X. Jin, D.F. Jin, X.L. Peng, J. Li, J. Gong, H.L. Ge, Z.W. Zhu, X.Q. Wang, Magnetic properties and adsorptive performance of manganese–zinc ferrites/activated carbon nanocomposites, J. Solid State Chem. 221 (2015) 302–305, https://doi.org/10.1016/j.jssc.2014.10.020.
[18] D.-W. Cho, J. Lee, Y.S. Ok, E.E. Kwon, H. Song, Fabrication of a novel magnetic carbon nanocomposite adsorbent via pyrolysis of sugar, Chemosphere 163 (2016) 305–312, https://doi.org/10.1016/j.chemosphere.2016.08.025.
[19] L. Ai, C. Zhang, Z. Chen, Removal of methylene blue from aqueous solution by a solvothermal-synthesized graphene/magnetite composite, J. Hazard Mater. 192 (2011) 1515–1524, https://doi.org/10.1016/j.jhazmat.2011.06.068.
[20] M. Namvari, H. Namazi, Magnetic sweet graphene nanosheets: preparation, characterization and application in removal of methylene blue, Int. J. Environ. Sci. Technol. 13 (2016) 599–606, https://doi.org/10.1007/s13762-015-0885-z.
[21] K.R. Thines, E.C. Abdullah, N.M. Mubarak, M. Ruthiraan, Synthesis of magnetic biochar from agricultural waste biomass to enhancing route for waste water and polymer application: a review, Renew. Sustain. Energy Rev. 67 (2017) 257–276, https://doi.org/10.1016/j.rser.2016.09.057.
[22] H. Huang, X. Liu, X. Zhang, W. Liu, X. Su, Z. Zhang, Fabrication of new magnetic nanoparticles (Fe3O4) grafted multiwall carbon nanotubes and heterocyclic compound modified electrode for electrochemical sensor, Electroanalysis 22 (2010) 433–438, https://doi.org/10.1002/elan.200900335.
[23] X. Liu, S. Zhang, H. Luo, Y. Zhang, Q. Xu, Z. Zhang, H. Xu, Z. Wang, Biomass activated carbon supported with high crystallinity and dispersion Fe3O4 nanoparticle for preconcentration and effective degradation of methylene blue, J. Taiwan Inst. Chem. Eng. 81 (2017) 265–274, https://doi.org/10.1016/j.jtice.2017.10.002.
[24] L. Guo, X. Cui, Y. Li, Q. He, L. Zhang, W. Bu, J. Shi, Hollow mesoporous carbon spheres with magnetic cores and their performance as separable bilirubin adsorbents, Chem. Asian J. 4 (2009) 1480–1485, https://doi.org/10.1002/asia.200900113.
[25] W.-K. Oh, H. Yoon, J. Jang, Size control of magnetic carbon nanoparticles for drug delivery, Biomaterials 31 (2010) 1342–1348, https://doi.org/10.1016/j.biomaterials.2009.10.018.
[26] A. Ahmad, S.H. Mohd-Setapar, C.S. Chuong, A. Khatoon, W.A. Wani, R. Kumar, M. Rafatullah, Recent advances in new generation dye removal technologies: novel search for approaches to reprocess wastewater, RSC Adv. 5 (2015) 30801–30818, https://doi.org/10.1039/C4RA16959J.
[27] S.L.F. López, M.R.M. Virgen, V.H. Montoya, M.A.M. Morán, R.T. Gómez, N.A.R. Vázquez, M.A.P. Cruz, M.S.E. González, Effect of an external magnetic field applied in batch adsorption systems: removal of dyes and heavy metals in binary solutions, J. Mol. Liq. 269 (2018) 450–460, https://doi.org/10.1016/j.molliq.2018.08.063.
[28] K.M. Lompe, D. Menard, B. Barbeau, Performance of biological magnetic powdered activated carbon for drinking water purification, Water Res. 96 (2016) 42–51, https://doi.org/10.1016/j.watres.2016.03.040.
[29] W. Fan, W. Gao, C. Zhang, W.W. Tjiu, J. Pan, T. Liu, Hybridization of graphene sheets and carbon-coated Fe3O4 nanoparticles as a synergistic adsorbent of organic dyes, J. Mater. Chem. 22 (2012) 25108–25115, https://doi.org/10.1039/C2JM35609K.
[30] P. González-García, Activated carbon from lignocellulosics precursors: a review of the synthesis methods, characterization techniques and applications, Renew. Sustain. Energy Rev. 82 (2018) 1393–1414, https://doi.org/10.1016/j.rser.2017.04.117.
[31] N. Yang, S. Zhu, D. Zhang, S. Xu, Synthesis and properties of magnetic Fe3O4-activated carbon nanocomposite particles for dye removal, Mater. Lett. 62 (2008) 645–647, https://doi.org/10.1016/j.matlet.2007.06.049.
[32] M. Zhang, B. Gao, S. Varnoosfaderani, A. Hebard, Y. Yao, M. Inyang, Preparation and characterization of a novel magnetic biochar for arsenic removal, Bioresour. Technol. 130 (2013) 457–462, https://doi.org/10.1016/j.biortech.2012.11.132.
[33] X. Gao, Y. Zhang, Y. Dai, F. Fu, High-performance magnetic carbon materials in dye removal from aqueous solutions, J. Solid State Chem. 239 (2016)

265–273, https://doi.org/10.1016/j.jssc.2016.05.001.
[34] L.C.A. Oliveira, R.V.R.A. Rios, J.D. Fabris, V. Garg, K. Sapag, R.M. Lago, Activated carbon/iron oxide magnetic composites for the adsorption of contaminants in water, Carbon N. Y. 40 (2002) 2177–2183, https://doi.org/10.1016/S0008-6223(02)00076-3.
[35] R. Kant, Textile dyeing industry an environmental hazard, Nat. Sci. (2012) 22–26, https://doi.org/10.4236/ns.2012.41004, 04.
[36] S. Gita, A. Hussan, T.G. Choudhury, Impact of textile dyes waste on aquatic environments and its treatment, Environ. Ecol. 35 (2017) 2349–2353.
[37] K.B. Tan, M. Vakili, B.A. Horri, P.E. Poh, A.Z. Abdullah, B. Salamatinia, Adsorption of dyes by nanomaterials: recent developments and adsorption mechanisms, Separ. Purif. Technol. 150 (2015) 229–242, https://doi.org/10.1016/j.seppur.2015.07.009.
[38] S. Cheng, L. Zhang, A. Ma, H. Xia, J. Peng, C. Li, J. Shu, Comparison of activated carbon and iron/cerium modified activated carbon to remove methylene blue from wastewater, J. Environ. Sci. 65 (2018) 92–102, https://doi.org/10.1016/j.jes.2016.12.027.
[39] T. Chen, Y. Xiong, Y. Qin, H. Yang, P. Zhang, F. Ye, Facile synthesis of low-cost biomass-based γ-Fe2O3/C for efficient adsorption and catalytic degradation of methylene blue in aqueous solution, RSC Adv. 7 (2017) 336–343, https://doi.org/10.1039/C6RA24900K.
[40] R. Wu, J.-H. Liu, L. Zhao, X. Zhang, J. Xie, B. Yu, X. Ma, S.-T. Yang, H. Wang, Y. Liu, Hydrothermal preparation of magnetic Fe3O4@C nanoparticles for dye adsorption, J. Environ. Chem. Eng. 2 (2014) 907–913, https://doi.org/10.1016/j.jece.2014.02.005.
[41] W. Jiang, L. Zhang, X. Guo, M. Yang, Y. Lu, Y. Wang, Y. Zheng, G. Wei, Adsorption of cationic dye from water using an iron oxide/activated carbon magnetic composites prepared from sugarcane bagasse by microwave method, Environ. Technol. (2019) 1–14, https://doi.org/10.1080/09593330.2019.1627425, 0.
[42] E. Altıntıg, H. Altundag, M. Tuzen, A. Sarı, Effective removal of methylene blue from aqueous solutions using magnetic loaded activated carbon as novel adsorbent, Chem. Eng. Res. Des. 122 (2017) 151–163, https://doi.org/10.1016/j.cherd.2017.03.035.
[43] H. Ma, J.-B. Li, W.-W. Liu, M. Miao, B.-J. Cheng, S.-W. Zhu, Novel synthesis of a versatile magnetic adsorbent derived from corncob for dye removal, Bioresour. Technol. 190 (2015) 13–20, https://doi.org/10.1016/j.biortech.2015.04.048.
[44] X. Zhu, Y. Liu, F. Qian, C. Zhou, S. Zhang, J. Chen, Preparation of magnetic porous carbon from waste hydrochar by simultaneous activation and magnetization for tetracycline removal, Bioresour. Technol. 154 (2014) 209–214, https://doi.org/10.1016/j.biortech.2013.12.019.
[45] X. Zhu, Y. Liu, C. Zhou, S. Zhang, J. Chen, Novel and high-performance magnetic carbon composite prepared from waste hydrochar for dye removal, ACS Sustain. Chem. Eng. 2 (2014) 969–977, https://doi.org/10.1021/sc400547y.
[46] G. Feiqiang, L. Xiaolei, J. Xiaochen, Z. Xingmin, G. Chenglong, R. Zhonghao, Characteristics and toxic dye adsorption of magnetic activated carbon prepared from biomass waste by modified one-step synthesis, Colloid. Surface. Physicochem. Eng. Aspect. 555 (2018) 43–54, https://doi.org/10.1016/j.colsurfa.2018.06.061.
[47] S. Gao, L. Liu, Y. Tang, D. Jia, Z. Zhao, Y. Wang, Coal based magnetic activated carbon as a high performance adsorbent for methylene blue, J. Porous Mater. 23 (2016) 877–884, https://doi.org/10.1007/s10934-016-0144-9.
[48] M.-M. Titirici, R.J. White, C. Falco, M. Sevilla, Black perspectives for a green future: hydrothermal carbons for environment protection and energy storage, Energy Environ. Sci. 5 (2012) 6796–6822, https://doi.org/10.1039/C2EE21166A.
[49] G. Yu, B. Sun, Y. Pei, S. Xie, S. Yan, M. Qiao, K. Fan, X. Zhang, B. Zong, Fe(x)O(y)@C spheres as an excellent catalyst for Fischer-Tropsch synthesis, J. Am. Chem. Soc. 132 (2010) 935–937, https://doi.org/10.1021/ja906370b.
[50] C. Falco, N. Baccile, M.-M. Titirici, Morphological and structural differences between glucose, cellulose and lignocellulosic biomass derived hydrothermal carbons, Green Chem. 13 (2011) 3273, https://doi.org/10.1039/c1gc15742f.
[51] Y. Qi, M. Zhang, L. Qi, Y. Qi, Mechanism for the formation and growth of carbonaceous spheres from sucrose by hydrothermal carbonization, RSC Adv. 6 (2016) 20814–20823, https://doi.org/10.1039/C5RA26725K.
[52] Y. Gong, H. Wang, Z. Wei, L. Xie, Y. Wang, An efficient way to introduce hierarchical structure into biomass-based hydrothermal carbonaceous materials, ACS Sustain. Chem. Eng. 2 (2014) 2435–2441, https://doi.org/10.1021/sc500447j.
[53] M. Sevilla, A.B. Fuertes, Chemical and structural properties of carbonaceous products obtained by hydrothermal carbonization of saccharides, Chem. Eur J. 15 (2009) 4195–4203, https://doi.org/10.1002/chem.200802097.
[54] W.-C. Qian, X.-P. Luo, X. Wang, M. Guo, B. Li, Removal of methylene blue from aqueous solution by modified bamboo hydrochar, Ecotoxicol. Environ. Saf. 157 (2018) 300–306, https://doi.org/10.1016/j.ecoenv.2018.03.088.
[55] N. Rattanachueskul, A. Saning, S. Kaowphong, N. Chumha, L. Chuenchom, Magnetic carbon composites with a hierarchical structure for adsorption of tetracycline, prepared from sugarcane bagasse via hydrothermal carbonization coupled with simple heat treatment process, Bioresour. Technol. 226 (2017) 164–172, https://doi.org/10.1016/j.biortech.2016.12.024.
[56] C. Falco, F. Perez Caballero, F. Babonneau, C. Gervais, G. Laurent, M.-M. Titirici, N. Baccile, Hydrothermal carbon from biomass: structural differences between hydrothermal and pyrolyzed carbons via 13C solid state NMR, Langmuir 27 (2011) 14460–14471, https://doi.org/10.1021/la202361p.
[57] F. Lu, L. Wen, J. Li, J. Wei, J. Xu, S. Zhang, Numerical simulation of iron whisker growth with changing oxygen content in iron oxide using phase-field method, Comput. Mater. Sci. 125 (2016) 263–270, https://doi.org/10.1016/j.commatsci.2016.09.003.
[58] M. Sevilla, G.A. Ferrero, A.B. Fuertes, One-Pot synthesis of biomass-based hierarchical porous carbons with a large porosity development, Chem. Mater. 29 (2017) 6900–6907, https://doi.org/10.1021/acs.chemmater.7b02218.
[59] M. Sevilla, G.A. Ferrero, A.B. Fuertes, Beyond KOH activation for the synthesis of superactivated carbons from hydrochar, Carbon N. Y. 114 (2017) 50–58, https://doi.org/10.1016/j.carbon.2016.12.010.
[60] X. Zhu, F. Qian, Y. Liu, D. Matera, G. Wu, S. Zhang, J. Chen, Controllable synthesis of magnetic carbon composites with high porosity and strong acid resistance from hydrochar for efficient removal of organic pollutants: an overlooked influence, Carbon N. Y. 99 (2016) 338–347, https://doi.org/10.1016/j.carbon.2015.12.044.
[61] X. Liu, M. Antonietti, Molten salt activation for synthesis of porous carbon nanostructures and carbon sheets, Carbon N. Y. 69 (2014) 460–466, https://doi.org/10.1016/j.carbon.2013.12.049.
[62] M. Sevilla, G.A. Ferrero, N. Diez, A.B. Fuertes, One-step synthesis of ultra-high surface area nanoporous carbons and their application for electrochemical energy storage, Carbon N. Y. 131 (2018) 193–200, https://doi.org/10.1016/j.carbon.2018.02.021.
[63] Y. Gong, H. Wang, Z. Wei, L. Xie, Y. Wang, An efficient way to introduce hierarchical structure into biomass- based hydrothermal carbonaceous materials, ACS Sustain. Chem. Eng. 2 (2014) 2435–2441, https://doi.org/10.1021/sc500447j.
[64] H. Zhang, L. Chen, L. Li, Y. Yang, X. Liu, Magnetic porous carbon microspheres synthesized by simultaneous activation and magnetization for removing methylene blue, J. Porous Mater. 24 (2017) 341–353, https://doi.org/10.1007/s10934-016-0267-z.
[65] A.L. Cazetta, O. Pezoti, K.C. Bedin, T.L. Silva, A. Paesano Junior, T. Asefa, V.C. Almeida, Magnetic activated carbon derived from biomass waste by concurrent synthesis: efficient adsorbent for toxic dyes, ACS Sustain. Chem. Eng. 4 (2016) 1058–1068, https://doi.org/10.1021/acssuschemeng.5b01141.
[66] C.F. Holder, R.E. Schaak, Tutorial on powder X-ray diffraction for characterizing nanoscale materials, ACS Nano 13 (2019) 7359–7365, https://doi.org/10.1021/acsnano.9b05157.
[67] D.L.A. de Faria, S.V. Silva, M.T. de Oliveira, Raman microspectroscopy of some iron oxides and oxyhydroxides, J. Raman Spectrosc. 28 (1997) 873–878, https://doi.org/10.1002/(SICI)1097-4555(199711)28:11%3C873::AID-JRS177%3E3.0.CO;2-B.
[68] J. Ma, Z. Zhu, B. Chen, M. Yang, H. Zhou, C. Li, F. Yu, J. Chen, One-pot, large-scale synthesis of magnetic activated carbon nanotubes and their applications for arsenic removal, J. Mater. Chem. A. 1 (2013) 4662–4666, https://doi.org/10.1039/C3TA10329C.
[69] M. Chen, L.-L. Shao, J.-J. Li, W.-J. Pei, M.-K. Chen, X.-H. Xie, One-step hydrothermal synthesis of hydrophilic Fe3O4/carbon composites and their application in removing toxic chemicals, RSC Adv. 6 (2016) 35228–35238, https://doi.org/10.1039/C6RA01408A.
[70] F. Martin-Hernandez, A.M. Hirt, Evidence for weak ferromagnetic moment within the basal plane of hematite natural crystals at low temperature, Geochem. Geophys. Geosyst. 14 (2013) 4444–4457, https://doi.org/10.1002/ggge.20245.
[71] G. Cinader, S. Shtrikman, Antiferromagnetic to weak ferromagnetic transition and the temperature dependence of the transverse susceptibility in hematite below the Morin transition, Solid State Commun. 4 (1966) 459–462, https://doi.org/10.1016/0038-1098(66)90329-2.
[72] D.L.a. de Faria, S. V Silva, M.T. de Oliveira, Raman microspectroscopy of some iron oxides and oxyhydroxides, J. Raman Spectrosc. 28 (1997) 873.
[73] A.C. Ferrari, D.M. Basko, Raman spectroscopy as a versatile tool for studying the properties of graphene, Nat. Nanotechnol. 8 (2013) 235–246, https://doi.org/10.1038/nnano.2013.46.
[74] A. Sadezky, H. Muckenhuber, H. Grothe, R. Niessner, U. Pöschl, Raman microspectroscopy of soot and related carbonaceous materials: spectral analysis and structural information, Carbon N. Y. 43 (2005) 1731–1742, https://doi.org/10.1016/j.carbon.2005.02.018.
[75] M. Pawlyta, J.-N. Rouzaud, S. Duber, Raman microspectroscopy characterization of carbon blacks: spectral analysis and structural information, Carbon N. Y. 84 (2015) 479–490, https://doi.org/10.1016/j.carbon.2014.12.030.
[76] M.O. Castro, M.Q. de Santiago, K.S. Nascimento, B. Sousa Cavada, E. de Castro Miguel, A.J. de Paula, O.P. Ferreira, Hydrochar as protein support: preservation of biomolecule properties with non-covalent immobilization, J. Mater. Sci. 52 (2017) 13378–13389, https://doi.org/10.1007/s10853-017-1441-7.
[77] M. Thommes, K. Kaneko, A.V. Neimark, J.P. Olivier, F. Rodriguez-reinoso, J. Rouquerol, K.S.W. Sing, Physisorption of gases , with special reference to the evaluation of surface area and pore size distribution, IUPAC Technical Report, https://doi.org/10.1515/pac-2014-1117, 2015, 87, 1051-1069.
[78] M. Li, W. Li, S. Liu, Hydrothermal synthesis, characterization, and KOH activation of carbon spheres from glucose, Carbohydr. Res. 346 (2011) 999–1004, https://doi.org/10.1016/j.carres.2011.03.020.
[79] M.-M. Titirici, R.J. White, C. Falco, M. Sevilla, Black perspectives for a green future: hydrothermal carbons for environment protection and energy storage, Energy Environ. Sci. 5 (2012) 6796, https://doi.org/10.1039/c2ee21166a.
[80] D. Tian, Z. Xu, D. Zhang, W. Chen, J. Cai, H. Deng, Z. Sun, Y. Zhou, Micro–mesoporous carbon from cotton waste activated by FeCl3/ZnCl2:

preparation, optimization, characterization and adsorption of methylene blue and eriochrome black T, J. Solid State Chem. 269 (2019) 580–587, https://doi.org/10.1016/j.jssc.2018.10.035.
[81] Y. Wu, J.-P. Cao, X.-Y. Zhao, Z.-Q. Hao, Q.-Q. Zhuang, J.-S. Zhu, X.-Y. Wang, X.-Y. Wei, Preparation of porous carbons by hydrothermal carbonization and KOH activation of lignite and their performance for electric double layer capacitor, Electrochim. Acta 252 (2017) 397–407, https://doi.org/10.1016/j.electacta.2017.08.176.
[82] G.F. Goya, T.S. Berquó, F.C. Fonseca, M.P. Morales, Static and dynamic magnetic properties of spherical magnetite nanoparticles, J. Appl. Phys. 94 (2003) 3520–3528, https://doi.org/10.1063/1.1599959.
[83] B.D. Cullity, C.D. Graham, Introduction to Magnetic Materials, second ed., Wiley-IEEE Press, 2009.
[84] R. Foroutan, R. Mohammadi, J. Razeghi, B. Ramavandi, Performance of algal activated carbon/Fe3O4 magnetic composite for cationic dyes removal from aqueous solutions, Algal Res. 40 (2019) 101509, https://doi.org/10.1016/j.algal.2019.101509.
[85] C. Chen, S. Mi, D. Lao, P. Shi, Z. Tong, Z. Li, H. Hu, Single-step synthesis of eucalyptus sawdust magnetic activated carbon and its adsorption behavior for methylene blue, RSC Adv. 9 (2019) 22248–22262, https://doi.org/10.1039/C9RA03490K.
[86] I. Shah, R. Adnan, W.S. Wan Ngah, N. Mohamed, Iron impregnated carbon materials with improved physicochemical characteristics, Mater. Sci. Eng. B Solid State Mater. Adv. Technol. 201 (2015) 1–12, https://doi.org/10.1016/j.mseb.2015.07.004.